Journal of CO2 Utilization 106 (2026) 103393

Contents lists available at ScienceDirect

Journal of CO2 Utilization

journal homepage: www.elsevier.com/locate/jcou

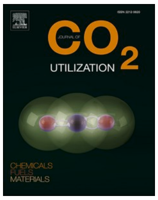

Effect of oxygen vacancies on the plasma-catalytic performance of CeO_2 for CO_2 hydrogenation

Joran Van Turnhout [a,b,c,d], Wouter Van Hoey [e], Shangkun Li [a,b,d,f], Robin De Meyer [a,b,d,g], Morgane Van Hove [a,e], Thomas Salens [b,g], Johan Verbeeck [b,g], Sara Bals [g], Bart Partoens [b,f], Emiel JM Hensen [c,*], Pegie Cool [e], Annemie Bogaerts [a,b,d,**]

[a] Research group PLASMANT, Department of Chemistry, University of Antwerp, Groenenborgerlaan 171, Antwerp 2020, Belgium
[b] Center of Excellence PLASMA, University of Antwerp, Groenenborgerlaan 171, Antwerp 2020, Belgium
[c] Laboratory of Inorganic Materials and Catalysis, Department of Chemical Engineering and Chemistry, Eindhoven University of Technology, P.O. Box 513, Eindhoven 5600 MB, the Netherlands
[d] Electrification Institute, University of Antwerp, Olieweg 97, Antwerp 2020, Belgium
[e] Research group LADCA, Department of Chemistry, University of Antwerp, Groenenborgerlaan 171, Antwerp 2020, Belgium
[f] Research group COMMIT, Department of Physics, University of Antwerp, Groenenborgerlaan 171, Antwerp 2020, Belgium
[g] Research group EMAT, Department of Physics, University of Antwerp, Groenenborgerlaan 171, Antwerp 2020, Belgium

ARTICLE INFO

Keywords:
Plasma catalysis
Oxygen vacancies
CO2 Hydrogenation
Dielectric barrier discharge

ABSTRACT

While plasma catalysis is a promising approach for sustainable chemical transformations, the fundamental mechanisms governing plasma–catalyst interactions remain elusive. In particular, the role of surface defects, such as oxygen vacancies (OVs) in metal oxide catalysts, on plasma-catalytic CO_2 hydrogenation is a subject of ongoing debate. To address this, we synthesized CeO_2 with varying surface OV concentrations through four pretreatment methods: (i) air calcination, (ii) Ar annealing, (iii) air calcination followed by in-situ reduction in H_2/Ar plasma, and (iv) air calcination followed by thermal H_2 reduction. These catalysts were evaluated in a temperature-controlled packed bed dielectric barrier discharge (DBD) reactor to isolate the impact of surface defects on plasma-catalytic CO_2 hydrogenation. Samples with higher OV concentrations exhibited lower CO_2 conversion, despite the conventional view that OVs promote CO_2 activation via a (reverse) Mars van Krevelen mechanism. We attribute this inhibition to a significant reduction in the number and intensity of micro-discharges. This shift is likely due to a decreased work function of CeO_2 following OV formation, which alters the plasma characteristics. In this regime, the modification of the alter the dominant gas phase chemistry appears to overshadow the expected surface catalytic effects. The introduction of Cu nanoparticles on CeO_2 further decreases CO_2 conversion, a result that correlates directly with a drop in the number and intensity of micro-discharges. These findings highlight the critical role of discharge-catalyst interactions in plasma catalysis, which is impacted by the OV concentration on CeO_2.

1. Introduction

Plasma catalysis has recently gained increasing interest as a promising technology in the fight against climate change. Its ability to be rapidly switched on and off makes plasma catalysis suitable for integration with intermittent renewable energy sources. However, plasma-catalytic gas conversion remains at a low technology readiness level (TRL), with many fundamental questions regarding the underlying mechanisms, hampering progress in the field [1].

One of the key questions in plasma catalysis pertains to the role of surface reactions. While most work focuses on surface reactions on transition metals [2,3], the contribution of oxide support materials is not always explicitly considered. In contrast, in thermal catalysis, it is well established that supports can participate in catalytic surface reactions [4,5]. Additionally, modelling work by Loenders et al. [6] showed that the use of transition metals in a plasma at 500 K for dry reforming of methane deteriorates system performance, because radicals generated in the plasma predominantly recombine back to the reactants at the

---

* Corresponding author.
** Corresponding author at: Research group PLASMANT, Department of Chemistry, University of Antwerp, Groenenborgerlaan 171, Antwerp 2020, Belgium.
E-mail addresses: e.j.m.hensen@tue.nl (E.J. Hensen), annemie.bogaerts@uantwerpen.be (A. Bogaerts).

https://doi.org/10.1016/j.jcou.2026.103393
Received 23 January 2026; Received in revised form 28 February 2026; Accepted 10 March 2026

transition metal surface. Furthermore, various experimental studies show that transition metal-based catalysts added to a plasma reaction zone can adversely affect overall system performance [7,8]. Hence, the need to explore different catalyst materials becomes clear.

In this regard, multivalent metal oxides are of particular interest due to their ability to accommodate oxygen vacancies (OVs) through surface reduction via the Mars van Krevelen (MvK) mechanism [9]. OVs are particularly relevant for CO_2 activation, as they enable the reverse MvK mechanism, where CO_2 is activated by occupying an OV to yield CO. Additionally, OVs may scavenge O radicals from the plasma, suppressing the recombination of O and CO to CO_2 in the plasma. By consuming these radicals, OVs suppress the back-reaction in the gas phase, thereby enhancing the CO_2 conversion [1]. Furthermore, these sites can be regenerated in-situ through surface reduction by H_2 or plasma-generated H species, forming H_2O byproduct. Thus, CeO_2 has been extensively explored for CO_2 activation in thermal catalysis [10,11]. However, its behavior under the complex influence of plasma discharge remains a subject of intensive study.

The literature about plasma-catalytic CO_2 activation on reducible metal oxides mentions several mechanisms. Parastaev et al.[12] used in-situ DRIFTS to demonstrate differences in thermo-catalytic and plasma-catalytic CO_2 hydrogenation on a Co/$CeZrO_4$ catalyst: OVs enhance CO_2 reduction through a formate pathway at the metal–support interface during thermal catalysis, whereas CO_2 hydrogenation occurs via the carbonyl pathway in the plasma, without involvement of OVs. For the latter case, the temperature must be increased substantially for the OVs to play a role in CO_2 hydrogenation at the metal-support interface. In contrast, Ning et al. [13] observed enhanced CO_2 conversion when a Cu/$CeZrO_4$ catalyst was placed in a dielectric barrier discharge (DBD) plasma reactor. The authors proposed a reaction mechanism involving hydrogen spillover from Cu nanoparticles to CO_2 adsorbed on OVs near the metal-support interface, followed by the reaction of excited H species with adsorbed CO_2 via an Eley–Rideal mechanism. Such a mechanism involving plasma-generated H species would not require the presence of a transition metal on the catalyst surface, preventing possible recombination reactions [6]. Nevertheless, the contribution of such a mechanism is probably minor, as the performance for a reactor filled with $CeZrO_4$ support without Cu nanoparticles was similar to the performance of the empty reactor. Golubev et al. [14] found that CO_2 dissociation in a DBD plasma is enhanced by the presence of MgO–CeO_2 catalysts, and the performance increased with higher CeO_2 content, likely involving CeO_2 OVs. Similarly, Ashford et al. [15] explained increased CO_2 dissociation in a plasma to OVs in CeO_2-promoted Fe-oxide catalysts. Cheng et al. [16] attributed the high CO_2 conversion and CO selectivity on Pd-WO_{3-x} supported on Ni foam to CO_2 activation on surface OVs. Despite these insightful studies, direct experimental evidence for the involvement of OVs in CeO_2 during plasma-catalytic CO_2 conversion is still lacking.

Moreover, recent studies by Ndayirinde et al. [8], De Meyer et al. [7] and Merino et al. [17] showed that discharge-related modifications dominate over true surface-catalytic effects in packed bed DBD reactors. However, this insight is often overlooked in much of the existing literature, which tends to focus primarily on catalytic surface interactions. As a result, it remains uncertain whether OVs enhance plasma-catalytic activity through direct involvement in surface reaction pathways or indirectly by altering the discharge characteristics, thereby affecting plasma chemistry.

To gain deeper insight into the role of OVs in plasma-catalytic CO_2 hydrogenation, this work investigates how different pretreatment methods of CeO_2, designed to modify the OV concentration, influence its plasma-catalytic performance. In addition, we examine the role of a transition metal (Cu) deposited onto the CeO_2 support to probe potential contributions from metal-support interfacial sites. A distinctive feature of this work is the integration of detailed plasma-electrical characterization to quantify the intensity and number of microdischarges, coupled with density functional theory (DFT) calculations. This approach allows us to evaluate how surface defects and metal deposition alter the catalyst function in plasma during CO_2 hydrogenation.

2. Methods

2.1. Catalyst synthesis

CeO_2 was synthesized by an adapted template-free and scaled-up procedure reported by Van Hoey et al. [18] First, 32.4 g of $CeCl_3 \bullet 7\ H_2O$ (99%, Merck) was dissolved in 450 ml of deionized water using a 1000 ml round-bottom flask. After complete dissolution, the round-bottom flask was placed in an oil bath, and the temperature was raised to 50 °C. Subsequently, 120 ml of a 12.5% NH_4OH solution was added dropwise. The resulting mixture was stirred overnight at 50 °C and then transferred to a 1 L stainless-steel autoclave pressure vessel with a Teflon liner, where it is kept at 100 °C for 24 h. Next, the obtained slurry was filtered, washed with distilled water and dried at room temperature.

To gain a better understanding of the influence of OVs on plasma-catalytic CO_2 hydrogenation, the surface OV concentration on CeO_2 was altered by applying four different approaches, as shown in Table 1. These treatments were selected to obtain a controlled gradient in surface OV concentration without significantly altering bulk structure. For CeO_2-PR and CeO_2-TR, prereduction is performed after thermal treatment. The duration of in-situ prereduction in H_2/Ar plasma was optimized through XPS measurements without air exposure to ensure the surface reached a steady state of reduction. To validate this, we reduced CeO_2 in-situ for 15 min and 30 min. The results showed no significant increase in the Ce^{3+} concentration between both time periods (14.3% for 15 min and 14.1% for 30 min), indicating that surface reduction reaches saturation within 15 min under these conditions. Ex-situ prereduction of CeO_2-TR was performed before the plasma-catalytic experiment to limit sample oxidation.

To examine the influence of the presence of Cu nanoparticles on the plasma-catalytic performance of CeO_2, Cu was deposited using an ammonia-driven deposition precipitation approach [19,20]. In this work, 6 g of calcined CeO_2 was suspended in 97.3 ml of 0.03 M copper nitrate solution to obtain a Cu loading of 3 wt%. Then, a desired amount of NH_4OH (28–30%, Acros) was added to the mixture to obtain a molar Cu:NH_3 ratio of 1:6. Subsequently, the corresponding solution was stirred for 48 h at room temperature, followed by filtration and washing with deionized water. After drying at room temperature, the obtained solid was calcined in air at 550 °C for 6 h at a heating rate of 1 °C min^{-1} and subsequently prereduced in-situ in H_2/Ar plasma (20 ml min^{-1} Ar, 20 ml min^{-1} H_2, 15 min, 24 W). The final sample is referred to as 3 wt% Cu/CeO_2.

For all samples, the catalyst powder was pelletized using a hydraulic press at 2 tons, then crushed and sieved to obtain a pellet size between 900 and 1250 μm.

2.2. Catalyst characterization

To determine the crystallographic structure of the materials, X-ray

Table 1
Experimental conditions for pretreatment and prereduction of the samples.

Sample name	Thermal pretreatment	Prereduction
CeO_2	Air 450 °C, 1 °C min^{-1}, 5 h	-
CeO_2-Ar	Ar 450 °C, 1 °C min^{-1}, 5 h	-
CeO_2-PR	Air 450 °C, 1 °C min^{-1}, 5 h	50% H_2/Ar plasma, in-situ 24 W, 15 min
CeO_2-TR	Air 450, 1 °C min^{-1}, 5 h	5% H_2/Ar, ex-situ 600 °C, 5 °C min^{-1}, 6 h 50% H_2/Ar plasma, in-situ 24 W, 15 min

diffraction (XRD) measurements were performed using a Bruker D8 Advance eco X-ray diffractometer equipped with CuKα radiation ($\lambda = 0.15406$ nm). The XRD patterns were recorded at 0.04 °/ s in the 2θ range of 5 ° to 80 °.

Raman spectra were recorded using a Micro-Raman Horiba instrument equipped with an xPlora Plus Microscope featuring a 50x objective magnification, equipped with a laser with a wavelength of 532 nm.

The specific surface area and pore size distribution of the catalysts were determined using N_2 porosimetry. The measurements were performed at a temperature of −196 °C using a Quantachrome Quadrasorb SI surface area and pore size analyzer. Before N_2-sorption measurements, the samples were degassed under vacuum during 16 h at a temperature of 200 °C using an AS-6 degasser.

Scanning electron microscopy (SEM) and energy dispersive X-ray spectroscopy (EDX) analyses were performed using a Thermo Fisher Scientific Quanta 250 ESEM equipped with an Oxford Instruments EDX detector. TEM measurements were performed using a Thermo Fisher Scientific Tecnai Osiris G20, operated at 200 kV in high-angle annular dark-field scanning TEM (HAADF-STEM) imaging mode. Prior to electron microscopy analyses, the samples were suspended in ethanol by sonication and vortexing, after which a few drops of the suspension were drop cast on an SEM stub or a holey carbon TEM grid which were left to dry under ambient conditions. For SEM analyses, a carbon coating of approximately 20 nm was applied after deposition of the sample on the SEM stub to avoid charging.

H_2-temperature programmed reduction (H_2-TPR) were performed using a CHEMSTAR TPx Chemisorption analyzer. 100 mg of sample was placed in a U-shaped tube and purged with Ar for 1 h at 50 °C, using a flow rate of 80 ml min^{-1}. Then, 5% of H_2/Ar was introduced using a flow rate of 30 ml min^{-1}. The temperature was increased linearly from 100 to 1000 °C at a heating rate of 10 °C min^{-1}. H_2 consumption was measured as a function of temperature by a thermal conductivity detector (TCD). The reported data was normalized per gram of catalyst. Finally, the H_2 consumption of each sample was determined using a pulse calibration method, whereby every minute, for a duration of 10 min, an additional pulse of 517 µl pure Ar was sent over the detector.

X-ray photoelectron spectroscopy (XPS) measurements were performed using a K-Alpha X-ray photoelectron spectrometer (Thermo Scientific) with a monochromatic X-ray source. Spectra were recorded using an aluminum (Al) anode (1486.68 eV) at 72 W with a spot size of 400 µm. The spectra were analyzed using CasaXPS software. The Ce 3d line was fitted to probe the OV concentration [21] according to a model described elsewhere [22,23]. The fit parameters (binding energies, peak areas, FWHM) are provided in Tables S2-S11. When measuring without exposure to air, valves on both ends of the reactor were closed after the experiment and the reactor was transferred to gas-tight containers in a glovebox, after which it was transferred to a gas-tight XPS holder.

Inductively coupled plasma optical emission spectroscopy (ICP-OES) was used for determining the Cu content of the 3 wt% Cu/CeO_2 sample, using a Spectroblue (AMETEK Inc.) spectrometer. Extraction was done by dissolving the sample in concentrated H_2SO_4 (98%) at 250 °C.

2.3. *Plasma-catalytic performance*

We conducted plasma-catalytic experiments in a temperature-controlled coaxial DBD reactor at atmospheric pressure (Fig. 1). The DBD reactor comprised two coaxial transparent glass cylinders, with water circulating in between at a flow rate of 5 L min^{-1} and a temperature of 308 K. A tungsten filament was integrated into the outer cylinder to ground the water. Hence, the water functioned as the ground electrode, and simultaneously kept the temperature of the reactor wall constant, limiting (local) overheating. The tungsten filament was connected to the ground through a capacitor (10 nF). The inner diameter of the reactor was 4 mm. A stainless-steel electrode with a diameter of 2 mm, used as the high-voltage (HV) electrode, was positioned at the center, yielding a discharge gap of 1 mm. The length of the discharge region was 100 mm. The catalyst sample was held in place by quartz wool at the bottom of the reactor, outside of the discharge zone. The sample was loaded into the reactor until the entire discharge region (0.9 cm^3) is filled, corresponding to ~1.5 g of catalyst material.

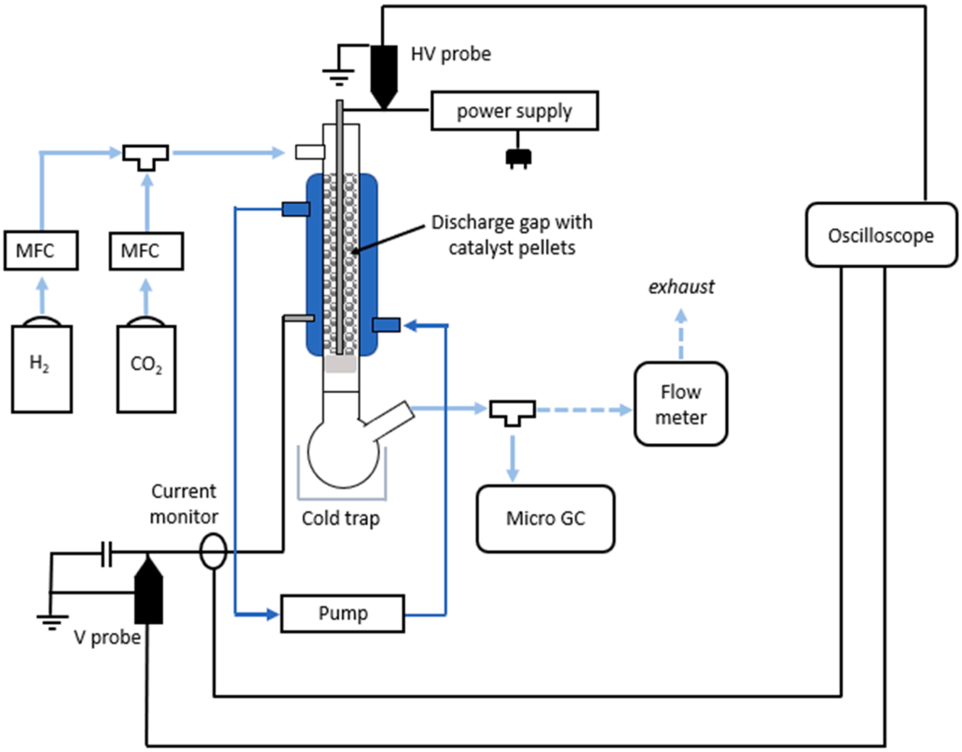

Fig. 1. Schematic representation of the used plasma reactor setup: a temperature-controlled coaxial DBD reactor was operated at atmospheric pressure to study plasma-catalytic CO_2 hydrogenation.

An AFS G10S-V2x power supply unit (PSU) sustained the discharge at a fixed frequency of 23.5 kHz. During the experiment, the plasma power was kept constant at ~ 26 W. The average power obtained for each experiment is provided in Table S1 in Supporting Information (SI). The applied voltage and the current were monitored with a digital oscilloscope (Pico Technology PicoScope 6402D) connected to a high-voltage probe (Tektronix P6015A) and a current monitor (Pearson Electronics 4100). The voltage over the capacitor was monitored by the oscilloscope through a low-voltage probe (Pico Technology TA150).

Mass flow controllers (Alicat Scientific and Bronkhorst), which were connected to an H_2 gas cylinder (99.999%, Air Liquide) and a CO_2 gas cylinder (99.999%, Air Liquide) introduced the feed gases H_2 and CO_2 into the reactor at a total flow rate of 40 ml min^{-1} and a 3:1 H_2 to CO_2 ratio. Downstream the reactor, the volumetric flow rate was continuously monitored using an Agilent Crosslab CS volumetric flow meter.

The outlet gas was analyzed using online gas chromatography (GC) (Agilent 990 MicroGC) equipped with a Molsieve 5 A column (CO, H_2, CH_4) preceded by a CP-PORABOND Q precolumn and a PORAPLOT U column preceded by a CP-PORABOND Q precolumn (CO_2). The calibration curves are provided in SI, section S1 (Figures S1-S4). The outflow of the reactor was first sent through a cold trap to avoid damage to the GC caused by condensed liquids.

Each experiment consisted of three runs. For every run, four initial blank gas composition measurements were recorded without plasma. Subsequently, ten gas composition measurements were recorded with plasma switched on, with each measurement taking 5 min. As steady state was reached almost immediately, the calculations of the activity metrics for each run were based on the average peak areas of these ten outlet measurements. Finally, the results for each experiment were obtained by calculating the average of its three respective runs. The error bars represent the standard deviation between the triplicates. For the CeO_2-PR and CeO_2-TR samples, only one run was performed due to the limited availability of the sample. The activity metrics presented in this work are the CO_2 conversion, H_2 conversion, CO selectivity and CH_4 selectivity, and were calculated using the formulas presented in Wanten & Vertongen et al. [24]

The conversion is defined as follows:

$$\chi_i = \frac{c_{i,\ inlet} - \alpha_{flux} * c_{i,\ outlet}}{c_{i,\ inlet}} * 100\% \text{with } i = CO_2 \text{or} H_2 \tag{1}$$

Here, α_{flux} is the flux ratio or volume expansion factor, which ensures gas expansion/contraction is accounted for in the calculation of the conversion. It is defined as follows:

$$\alpha_{flux} = \frac{\dot{n}_{tot}^{out}}{\dot{n}_{tot}^{in}} = \frac{\dot{V}_{tot}^{out}}{\dot{V}_{tot}^{in}} \tag{2}$$

For the calculation of α_{flux}, the volumetric flow rate was measured before ignition of the plasma ($\dot{V}_{tot}^{in}$). During a typical reaction experiment, three volumetric flow rate measurements were recorded every 15 min ($\dot{V}_{tot}^{out}$), and the average was used to calculate α_{flux} for the experimental run.

The carbon- or hydrogen-based selectivity of product *j* based on atom A = C or H is defined as follows:

$$S_j^A = \frac{\nu_j^A * \alpha_{flux} * c_j^{out}}{\sum_i \nu_i^A \left(c_i^{in} - \alpha_{flux} * c_i^{out}\right)} * 100\% \text{with } j = CO \text{ or } CH_4 \tag{3}$$

with ν_j^A the number of atoms *A* in product *j* and ν_i^A the number of atoms *A* in reactant *i.*

2.4. Discharge electrical characterization

During each plasma-catalytic experiment, the applied voltage, measured current and voltage across the monitoring capacitor were recorded every 15 min using an oscilloscope. These data were used to calculate the plasma power (P), the microdischarge quantity (see below), the cell capacitance (C_{cell}) and the dielectric capacitance (C_{diel}).

In this work, the plasma power for every snapshot was calculated as follows:

$$P = \frac{1}{T}\int_0^T V(t) * I(t)dt \tag{4}$$

with T the total time of the oscilloscope window, corresponding to N full periods of the applied voltage, V the applied voltage and I the measured current. The average power was calculated from 12 snapshots taken during the duration of the experiment.

C_{cell} can be extracted from the Lissajous figures, i.e. the charge–voltage (Q-V) diagram, by fitting a straight line to the “plasma off” phase of the Lissajous plot. The gradient of this line is C_{cell}, as shown in Figure S5 in SI [25]. Similarly, C_{diel} can be calculated by fitting a straight line to the “plasma on” phase of the Lissajous plot, as also shown in Figure S5.

The microdischarge quantity was introduced by De Meyer et al. [7] as an objective metric to quantify the number and intensity of microdischarges in a DBD plasma. It is obtained by applying a fast Fourier transform to the plasma current signal, followed by integration over the 10–100 MHz frequency range. A detailed description of the calculation procedure and its underlying assumptions is provided in De Meyer et al. [7]. Although the microdischarge quantity does not have a straightforward physical interpretation, it enables consistent comparison between experiments with various catalyst samples. Therefore, it is presented in arbitrary units. A higher microdischarge quantity corresponds to more microdischarges and/or microdischarges with a higher intensity.

2.5. DFT calculations

To study the effect of the surface OV concentration on the work function (WF) of CeO_2, spin-polarized density functional theory (DFT) calculations are performed using the Vienna Ab initio Simulation Package (VASP, version 6.2.1) [26–28]. The exchange-correlation interactions are described by the Perdew−Burke−Ernzerhof (PBE) functional [29]. The projected augmented wave (PAW) method is employed [30,31]. A plane-wave cutoff energy of 500 eV is used to treat the valence electrons. To adequately describe electron localization in the Ce 4 f orbitals, on-site Coulomb interactions are included via the Hubbard U approach [32]. The U value is set to 4.5 eV for the Ce 4 f orbitals, providing sufficient localization for the electrons left on CeO_2[33–35]. The maximum force criterion for ionic convergence is set to 0.02 eV/Å. Van der Waals dispersion interactions between adsorbates and surfaces are accounted for using the Grimme DFT-D3 method with zero damping [36]. Brillouin zone integrations for bulk CeO_2 are performed using a 6 × 6 × 6 Monkhorst–Pack k-point mesh. The optimized lattice parameter for bulk CeO_2 is 5.47 Å, which is in reasonable agreement with the experimental value of 5.41 Å [37]. The CeO_2(111) surface is modeled by three O−Ce−O triple-layers with a (4 × 4) in-plane supercell, with a vacuum layer of 15 Å. The bottom O−Ce−O layers are fixed, while the top two O−Ce−O layers are allowed to relax. For surface calculations, only Γ-point sampling is used, together with a Gaussian smearing width of 0.05 eV.

3. Results and discussion

3.1. Catalyst characterization

The main physicochemical characteristics of CeO_2, CeO_2-Ar, CeO_2-PR, CeO_2-TR, and the Cu-containing 3 wt% Cu/CeO_2 sample are presented in Table 2.

The N_2 physisorption isotherms of all samples are depicted in Figure S6, and the corresponding BET surface areas are listed in Table 2. Interparticle porosity, characteristic for CeO_2 synthesized under

Table 2

Physicochemical properties of CeO_2 samples used in this study.

Catalyst	Average Crystallite size (nm)[a]	S_{BET} (m^2/g)[b]	H_2 consumption (μmol/g H_2)[c]	Cu loading (wt%)[d]
CeO_2	10.8	61	1167	-
CeO_2-Ar	9.4	77	1044	-
CeO_2-PR	9.2	66	-	-
CeO_2-TR	11.8	55	-	-
3 wt% Cu/ CeO_2	11.9	25	1573	3.1

[a] determined by XRD, [b] determined by N_2-sorption, [c] determined by H_2-TPR and [d] determined by ICP-OES analysis.

hydrothermal conditions, is confirmed by the steep increase in the adsorbed volume near a relative pressure of 0.90 and the presence of a type H1 hysteresis loop [18]. CeO_2, CeO_2-Ar, and CeO_2-PR exhibit comparable BET surface areas, in line with their similar average crystalline sizes as determined by XRD. CeO_2-TR shows a slight decrease in BET surface area, likely due to sintering induced by the thermal reduction process. Cu deposition onto the CeO_2 support reduces the surface area to 25 m^2/g, while the isotherm shape and hysteresis type remain unchanged, as shown in Figure S6.

XRD shows that CeO_2, CeO_2-Ar, CeO_2-TR, CeO_2-PR, and 3 wt% Cu/ CeO_2 exhibit the cubic fluorite-like crystal structure. Compared to calcination in air, thermal treatment of CeO_2 under Ar and plasma prereduction have a minor effect on the crystallite size (Table 2). CeO_2-TR shows a slightly increased crystallite size, likely due to sintering induced by thermal reduction. No identifiable CuO diffraction peaks are visible in the diffractogram of 3 wt% Cu/CeO_2, indicating high dispersion.

Figure S8 shows TEM images obtained from all samples, indicating that primary CeO_2 nanoparticles stick together in larger agglomerates, regardless of the pretreatment. STEM-EDX mapping of the Cu/CeO_2 sample (Figure S9) shows that Cu is present in specific regions, but these do not correspond to well-defined structures in the HAADF-STEM images, likely because the CuO particles are very small. The high Cu dispersion is further confirmed by the absence of CuO peaks in the XRD pattern of 3 wt% Cu/CeO_2. SEM images (Figure S10) reveal agglomerates of these smaller CeO_2 particles in all samples, without discernable difference between the samples at this scale. Accurately determining the particle size distributions for this sample morphology is not feasible, as this requires unambiguous identification of individual particles. Due to the high interparticle porosity and extensive agglomeration of smaller primary particles, the boundaries between individual particles cannot be objectively distinguished.

The Raman spectra of all five samples (Figure S11) contain an intense band centered around 460 cm^{-1}, attributed to the F_{2g} Raman mode of CeO_2. The appearance of a shoulder between 520 and 680 cm^{-1}, also referred to as the defect-induced band or D-band, indicates the relaxation of symmetry rules due to structural defects[21]. Nevertheless, this feature cannot be used to quantify defect densities. The deposition of Cu causes peak a red shift and broadening of the F_{2g} band[1], indicating weakening of the Ce-O bonds due to the presence of CuO. Finally, two shoulders appearing around 350 cm^{-1} and 630 cm^{-1} can be assigned to CuO [38].

The TPR profile of CeO_2 (Figure S12) contains two main reduction features at 530 °C and 780 °C with a broad shoulder between 300 and 460 °C. The peak at 530 °C can be attributed to the surface reduction of Ce^{4+} to Ce^{3+}, while the peak at 780 °C belongs to bulk CeO_2 reduction [39]. The shoulder before the first main reduction peak indicates the presence of more easily reducible sites at the surface of CeO_2. The fact that Ar calcination retains more OVs is supported by the almost absent shoulder in the reduction profile of CeO_2-Ar. Consequently, CeO_2-Ar exhibits a higher onset temperature for reduction (360 °C) compared to CeO_2 (300 °C). Additionally, the finding that CeO_2-Ar contains a higher OV concentration compared to CeO_2 is supported by comparing the total H_2 consumption: CeO_2-Ar required less H_2 for its complete reduction (1044 μmol/g) than CeO_2 (1167 μmol/g H_2). For 3 wt% Cu/CeO_2, three additional reduction signals are visible around 204 °C, 245 °C and 292 °C, respectively. The peak at 204 °C, which exhibits a shoulder between 105 °C and 180 °C, represents the reduction of well-dispersed Cu particles. The peak at 245 °C can be attributed to the presence of slightly larger CuO particles formed during the drying step. The peak around 292 °C can be assigned to a Cu-CeO_2 solid solution [40,41]. Due to the presence of CuO, the H_2 consumption of 3 wt% Cu/CeO_2 is higher (1573 μmol/g) than that of CeO_2 (1167 μmol/g).

Fig. 2 shows the fitted XPS spectra along with the surface Ce^{3+} fraction, used here as a proxy for OVs. All pretreatments increase the OV concentration. Replacing air calcination with thermal treatment in Ar raises the Ce^{3+} fraction from 12.9% to 14.7%, and a comparable increase is observed after in-situ H_2/Ar plasma pretreatment. For CeO_2-PR and CeO_2-TR, spectra were acquired without exposure to air, to determine the effective OV concentration in the sample after in-situ prereduction. Among the protocols, thermal prereduction yields the highest Ce^{3+} fraction of 16%. As XPS can induce partial reduction of Ce^{4+}, the reported Ce^{3+} values should be interpreted qualitatively, allowing for comparison between samples but not providing absolute Ce^{3+} fractions (see also section S2.6).

It should be noted that the OV concentration on a catalyst surface can change during reaction: an oxidative atmosphere typically decreases the OV concentration, whereas a reductive environment increases it, particularly on reducible oxide supports. Measuring the OV concentration during the reaction requires in-situ XPS, which is not yet available for plasma-catalytic systems. To estimate these changes, we measured the XPS spectrum of the spent catalysts without exposure to air (Figures S14-S18). The results indicate a slight rise in OV concentration for all samples after reaction, while the general trend remains. Only for CeO_2-Ar, the OV concentration of the spent catalyst breaks the trend, as this sample shows the highest OV concentration (17.0%). We attribute this to an inhomogeneous distribution of OVs on the surface, caused by the filamentary plasma behavior. Future experiments with highly time- and space-resolved in-situ characterization could enable a better understanding of the evolution of the OV concentration during the plasma-catalytic process.

Overall, these results confirm that the pretreatment methods primarily modify surface defects while preserving bulk structure, enabling isolation of OV effects on plasma-catalytic performance.

3.2. Plasma-catalytic activity

3.2.1. CeO_2

Initial online analysis without a cold trap and with heated gas transfer lines showed that CH_3OH in the effluent was below the GC detection limit. Accordingly, in the remainder of this work we report gas-phase CO and CH_4 products, while H_2O and any oxygenates are removed in the cold trap downstream of the reactor. The carbon balance is likely not closed due to deposition of carbonaceous products in the plasma zone.

The plasma-catalytic performance of CeO_2 is presented in Fig. 3. Compared to the reference empty reactor, packing the reactor with the samples enhances both CO_2 and H_2 conversion, while the CO and CH_4 selectivity are not significantly altered. For all samples, CO is the main reaction product, showing that the reverse water-gas shift (RWGS) reaction dominates. However, it is not always straightforward to compare the performance of an empty DBD reactor with a packed DBD reactor. On the one hand, the residence time in a packed reactor, at the same flow rate, is different from the empty reactor due to the reduced volume. Even if the flow rate was varied to keep the residence time constant, the specific energy input (SEI, the ratio of power over flow rate) would strongly change, affecting plasma-based gas conversion. On the other hand, the plasma-discharge characteristics change significantly upon

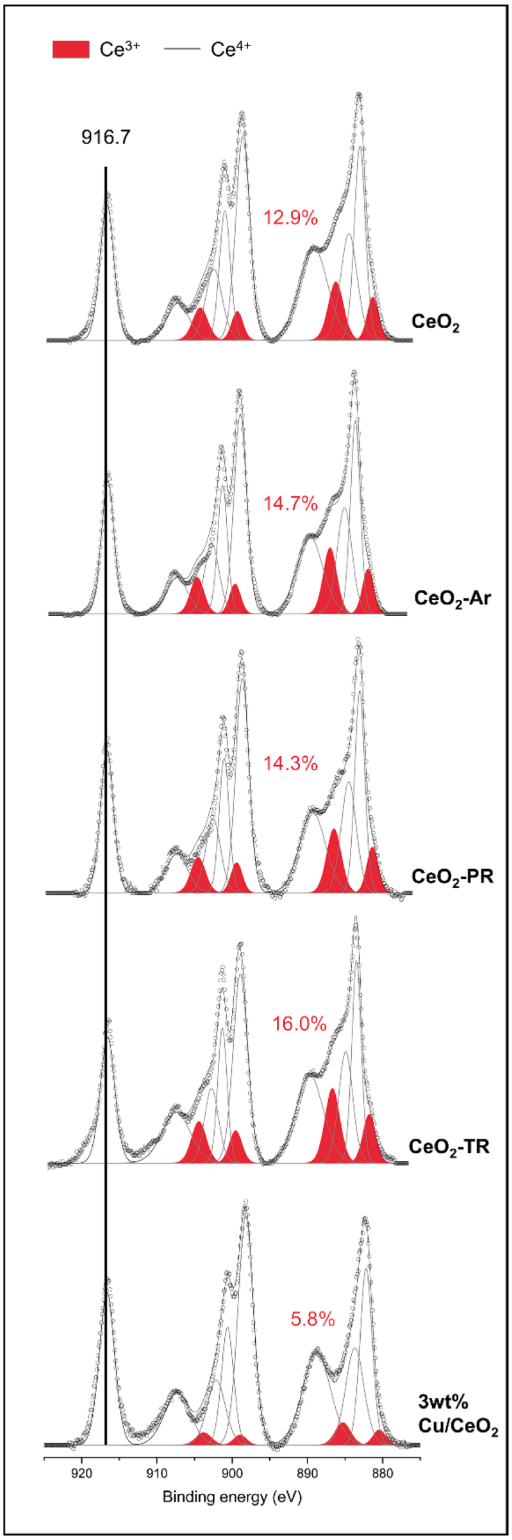

Fig. 2. XPS of Ce 3d for the CeO_2 samples and the 3 wt% Cu/CeO_2 sample. The spectra are normalized for visualization. All pretreatment methods effectively increase the OV concentration on the surface.

packing the reactor [8]. Therefore, this comparison should be made with caution [42].

The CeO_2 sample shows the highest CO_2 conversion, followed by CeO_2-Ar, CeO_2-PR, and CeO_2-TR. Notably, the surface OV concentration is inversely correlated with the CO_2 conversion (Fig. 3). This contrasts with the common hypothesis that the OV concentration enhances CO_2 activation through the reverse MvK mechanism, or prevent the recombination of CO and O.

To study the physical changes induced by the varying OV concentration, we extracted C_{cell} from the Lissajous figures recorded during the experiments. As C_{cell} is affected by changes in the dielectric constant of the material in the discharge gap, changes in the oxygen defect concentration may lead to variations in C_{cell}[43]. Fig. 4 shows C_{cell} as a function of time for the above samples. The accompanying Lissajous figures, current-voltage plots, and C_{diel} are given in section S3. While there is a small, but statistically significant difference in C_{diel} between CeO_2-TR and the other samples (Figure S20), the Lissajous figures show that the discharges behave similarly (Figure S21). As illustrated in Fig. 4, there is no significant difference in C_{cell} between the samples, indicating that any differences in dielectric constants between the samples are not sufficient to significantly alter C_{cell}. Moreover, there is no significant evolution of C_{cell} as a function of time, suggesting that the bulk is not significantly impacted throughout the experiment. Thus, a change in dielectric constant is not a sufficient explanation for the difference in CO_2 conversion.

While the bulk materials do not seem to differ significantly based on C_{cell}, the surfaces do, as is clear from the measured surface OV concentrations by XPS (Fig. 2). Earlier work by De Meyer et al. [7] showed that changing the surface properties of identical bulk materials can significantly alter the discharge homogeneity. This discharge homogeneity can be quantified by the microdischarge quantity (see Methods Section 2.4). Fig. 5 correlates the microdischarge quantity to the CO_2 conversion for the different samples. The larger uncertainty in the microdischarge quantity for the empty reactor is due to the greater discharge variability in the absence of packing, compared to the packed reactor.

The microdischarge quantity follows the same trend as the CO_2 conversion. This result aligns with the work by De Meyer et al., [7] who showed that, for dry reforming of methane, CO_2 activation in a packed bed DBD can be significantly enhanced by increasing the microdischarge quantity. Nevertheless, in the present study, the microdischarge quantity is negatively correlated with the OV concentration. CeO_2 yields a microdischarge quantity of 0.748 ± 0.001, which gradually decreases with increasing OV concentration, down to a microdischarge quantity of 0.40 ± 0.01 for CeO_2-TR. To understand this correlation, we performed DFT calculations, which are presented below.

3.2.2. Cu/CeO_2

Besides the metal-free CeO_2 samples, we also studied a Cu/CeO_2 sample, as the deposition of Cu nanoparticles could enable reactions either at the Cu surface or at the metal-support interface [40]. Fig. 6 illustrates the results of our plasma-catalytic activity experiments on Cu/CeO_2. Clearly, both the CO_2 and H_2 conversions decrease substantially upon loading CeO_2 with Cu. This further supports the conclusion that the reverse MvK mechanism does not play a dominant role. Although our H_2-TPR results show that 3 wt% Cu/CeO_2 exhibits significantly increased reducibility due to the hydrogen spillover effect, this increased reducibility does not translate into higher CO_2 conversion.

From Fig. 6, it is again evident that the CO_2 conversion correlates closely with the microdischarge quantity. The microdischarge quantity for the reactor loaded with Cu/CeO_2 (0.3744 ± 0.0006) is much lower than that for the reactor loaded with CeO_2 (0.748 ± 0.001). To understand the origin of this reduction in microdischarge quantity, we performed DFT calculations (Section 3.3).

3.3. DFT calculations

DFT calculations were performed to elucidate the impact of OV concentration and the presence of Cu on the electronic structure of CeO_2. First, we compared the electronic properties of pristine and modified stable $CeO_2(111)$ surfaces [44] We modeled defective surfaces with an OV created by removing a surface O atom (Fig. 10a) and a Cu-modified

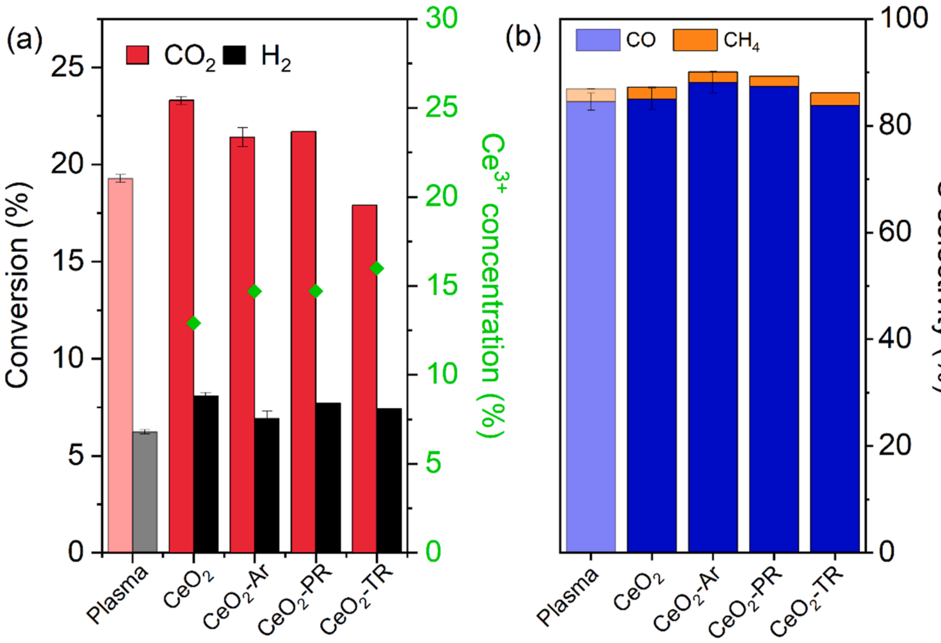

Fig. 3. (a) CO_2 and H_2 conversion along with the Ce^{3+} concentration obtained from XPS as a proxy for the OV concentration, and (b) C-based selectivity to CO and CH_4, obtained for the empty DBD reactor and the packed DBD filled with the four different CeO_2 samples, all in the temperature-controlled reactor (23.5 kHz, 26 W, 35 °C, total flow rate of 40 ml min^{-1} with CO_2:H_2 = 3:1). Error bars are not shown for CeO_2-PR and CeO_2-TR because only one experimental run could be performed for these samples. With an increase in Ce^{3+} concentration comes a decrease in CO_2 conversion, while the CO and CH_4 selectivities remain almost unchanged.

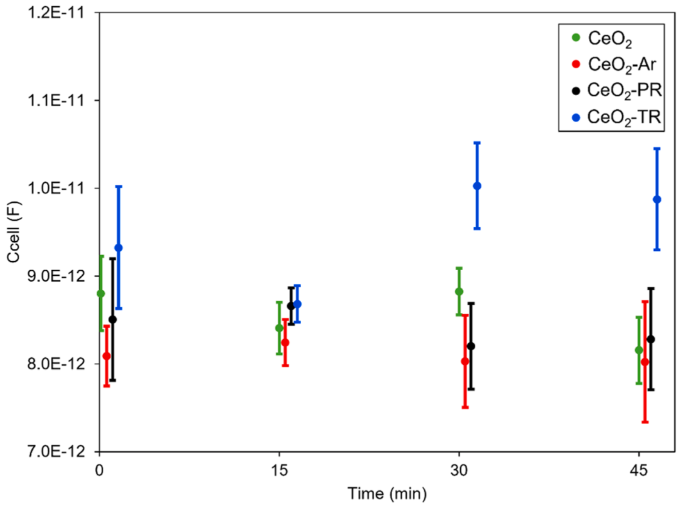

Fig. 4. C_{cell} extracted from the Lissajous figures recorded during the experiments with the four different samples (see legend). Note that all measurements are taken at the same time points (0, 15, 30 and 45 min) but are slightly shifted in the graph to improve legibility. There is no significant difference in C_{cell} between the samples, indicating that any differences in dielectric constants between the samples are not sufficient to significantly alter C_{cell}.

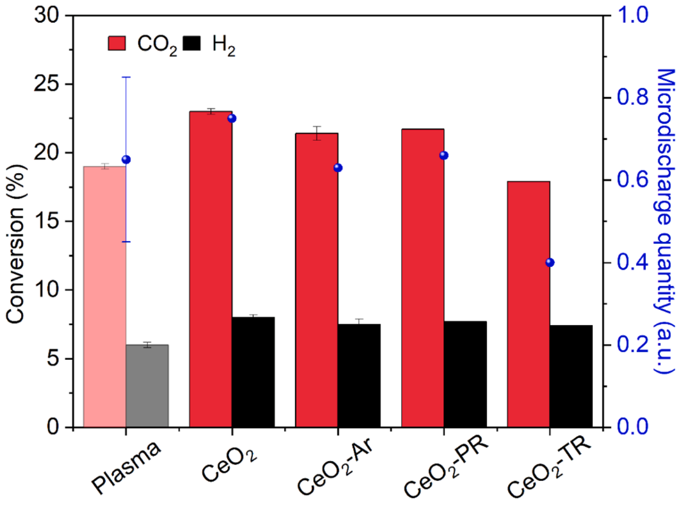

Fig. 5. CO_2 and H_2 conversions, along with microdischarge quantity, obtained for the empty DBD reactor and the packed DBD filled with the four different CeO_2 samples in the temperature-controlled reactor (23.5 kHz, 26 W, 35 °C, total flow rate of 40 ml min^{-1} with CO_2:H_2 = 3:1). Error bars are not shown for CeO_2-PR and CeO_2-TR because only one experimental run could be performed for these samples. Error bars on the microdischarge quantity in the packed bed reactor are in the order of 0.001, hence too small to be visible. The microdischarge quantity follows the same trend as the CO_2 conversion.

surface with a single Cu atom adsorbed at the most stable hollow site (Fig. 10b) [45]. Fig. 10(c–e) compare the total and projected density of states (TDOS and PDOS) of pristine $CeO_2(111)$, $CeO_2(111)$–OV1, and $Cu_1/CeO_2(111)$. For pristine $CeO_2(111)$, a clear band gap of about 2.21 eV is observed, with the valence band mainly composed of O 2p states and the conduction band dominated by Ce 4 f states. Upon introduction of an OV, defect-induced states emerge within the band gap, primarily associated with Ce 4 f orbitals of the reduced Ce^{3+} species neighboring the vacancy, resulting in a pronounced narrowing of the effective band gap. Similarly, adsorption of a single Cu atom on $CeO_2(111)$ leads to additional electronic states near the Fermi level, arising from strong hybridization between Cu 3d states and the surrounding Ce 4 f and O 2p states. This further enhances the electronic density near the Fermi level and significantly modifies the surface electronic structure.

Next, we investigated the WF, derived from the difference between the vacuum level from the electrostatic potential and the Fermi energy, as a function of the surface OV concentration. Therefore, two extra CeO_2 slabs $CeO_2(111)$–OV2 and $CeO_2(111)$–OV3 were constructed, with 2 and 3 OVs at the surface. Fig. 10 f shows the corresponding planar-

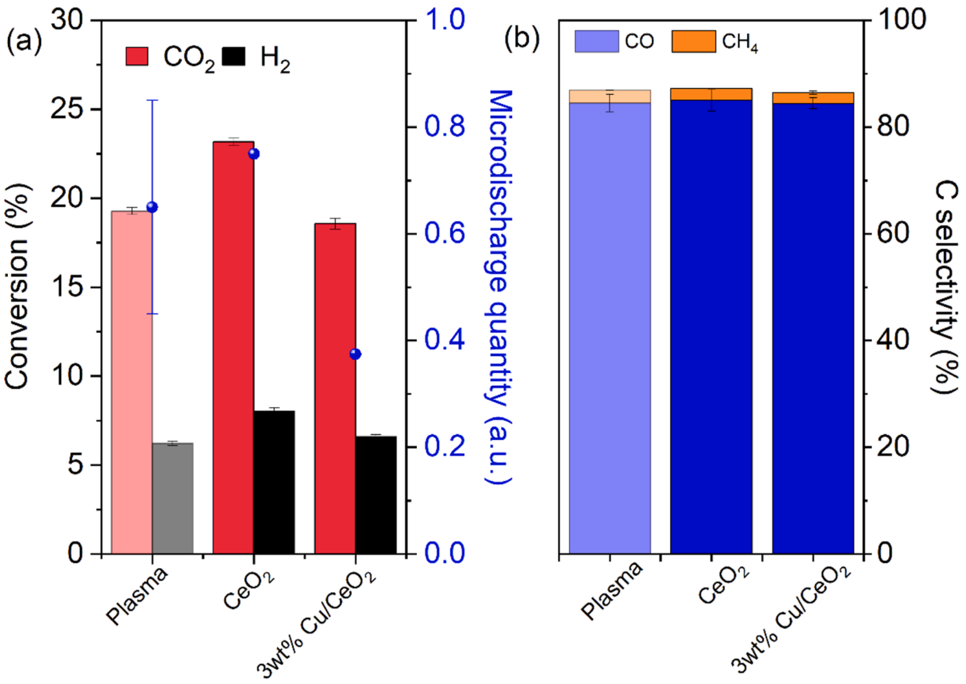

Fig. 6. (a) CO_2 and H_2 conversions, along with microdischarge quantity, and (b) C-based selectivity, obtained for the 3 wt% Cu/CeO_2 sample in the temperature-controlled packed bed DBD (23.5 kHz, 26 W, 35 °C, total flow rate of 40 ml min^{-1} with CO_2:H_2 = 3:1). Results for plasma-only and CeO_2 are displayed for reference. Error bars on the microdischarge quantity for the packed bed DBD are in the order of 0.001, hence too small to be visible. A decreased microdischarge quantity for 3 wt% Cu/CeO_2 leads to a decrease in CO_2 conversion, while the CO and CH_4 selectivity remains unchanged.

averaged electrostatic potential profiles, in which the introduction of OVs on the CeO_2(111) surface induces a downward shift of the vacuum level relative to the Fermi energy, leading to a progressive reduction of the WF as the OV concentration increases from OV1 to OV3 (Fig. 10 h). It should be mentioned that the jump in the vacuum level arises from OV-induced surface dipoles caused by charge redistribution and asymmetric defect placement, which shift the electrostatic potential in the vacuum region. Indeed, when OVs are introduced symmetrically on both sides of the CeO_2(111) slab, the vacuum level shift becomes negligible (Fig. 10 g). Moreover, Fig. 10 h also illustrates that the WF reduces under Cu addition (Figure S19).

To conclude, our DFT results indicate that both OVs and Cu adsorption lead to the appearance of defect levels within the band gap of CeO_2(111), resulting in an increase in electronic states near the Fermi level.

3.4. Discussion

A key finding of this work is that the OV concentration on the CeO_2 surface significantly influences the microdischarge quantity during plasma-catalytic CO_2 hydrogenation. Our DFT calculations demonstrate that an increase in the surface OV concentration introduces defect levels within the CeO_2(111) band gap and increases electronic states near the Fermi level, thereby lowering the WF [46,47]. These modified physical properties influence fundamental plasma processes, such as secondary electron emission [48], surface Penning ionization [49,50], field emission [51], and propagation of surface ionization waves [52,53], thereby modifying the discharge behavior. Specifically, we hypothesize that a lower WF, associated with a higher OV concentration, enhances electron seeding [7], which may promote a more uniform plasma with a lower microdischarge quantity. However, further fundamental studies are needed to isolate the exact mechanism by which material properties dictate discharge formation, particularly as subtle morphological changes in the catalyst may also contribute.

In turn, these discharge modifications significantly impact the overall CO_2 conversion. Earlier work by Snoeckx et al. [54] showed that CO_2 activation in a DBD plasma primarily proceeds through intense microdischarges, owing to the high electron-impact dissociation energy of CO_2 (~8.3 eV). Consequently, the observed decrease in CO_2 conversion with increasing OV concentration can be attributed to the corresponding reduction in microdischarge quantity, which suppresses gas-phase CO_2 activation. Our results therefore indicate that discharge-induced changes in the gas-phase chemistry govern the overall CO_2 conversion, largely overshadowing direct surface catalytic effects. After deposition of Cu on CeO_2 (3 wt% Cu/CeO_2), the CO_2 conversion decreases further. Although the OV concentration is lower for 3 wt% Cu/CeO_2 (5.8%), the introduction of metallic nanoparticles onto CeO_2 likely alters the same fundamental physical processes, modifying discharge characteristics. Supporting this, our DFT calculations show that Cu atoms on the CeO_2(111) surface lowers the WF.

The recombination of CO and O into CO_2 on Cu may also contribute to the observed decrease in CO_2 conversion. This is supported by microkinetic modelling by Loenders et al. [6] which revealed that in dry reforming of methane, the addition of a transition metal can hinder CO_2 conversion by facilitating recombination of CO and O rather than promoting CO_2dissociation. Furthermore, the enhanced CH_4 dissociation on Cu suggests an alternative pathway that may account for the reduced H_2 conversion. The simultaneous occurrence of these parallel reactions likely establishes a steady state, resulting in the observed constant selectivities for CO and CH_4. Developing a detailed, coupled plasma-surface kinetic model for plasma-catalytic CO_2 hydrogenation would be essential to further quantify the contributions of these specific pathways.

Furthermore, while the 3 wt% Cu/CeO_2 sample shows a significant reduction in surface area, this is likely not the primary cause of the diminished performance. In plasma catalysis, total surface area is generally not a determining factor for activity; reactive plasma species are typically not generated within small catalyst pores, and their diffusion into the internal pore structure is hindered by their short lifetime [1]. Other experiments we performed with a 6 wt% Cu loading support

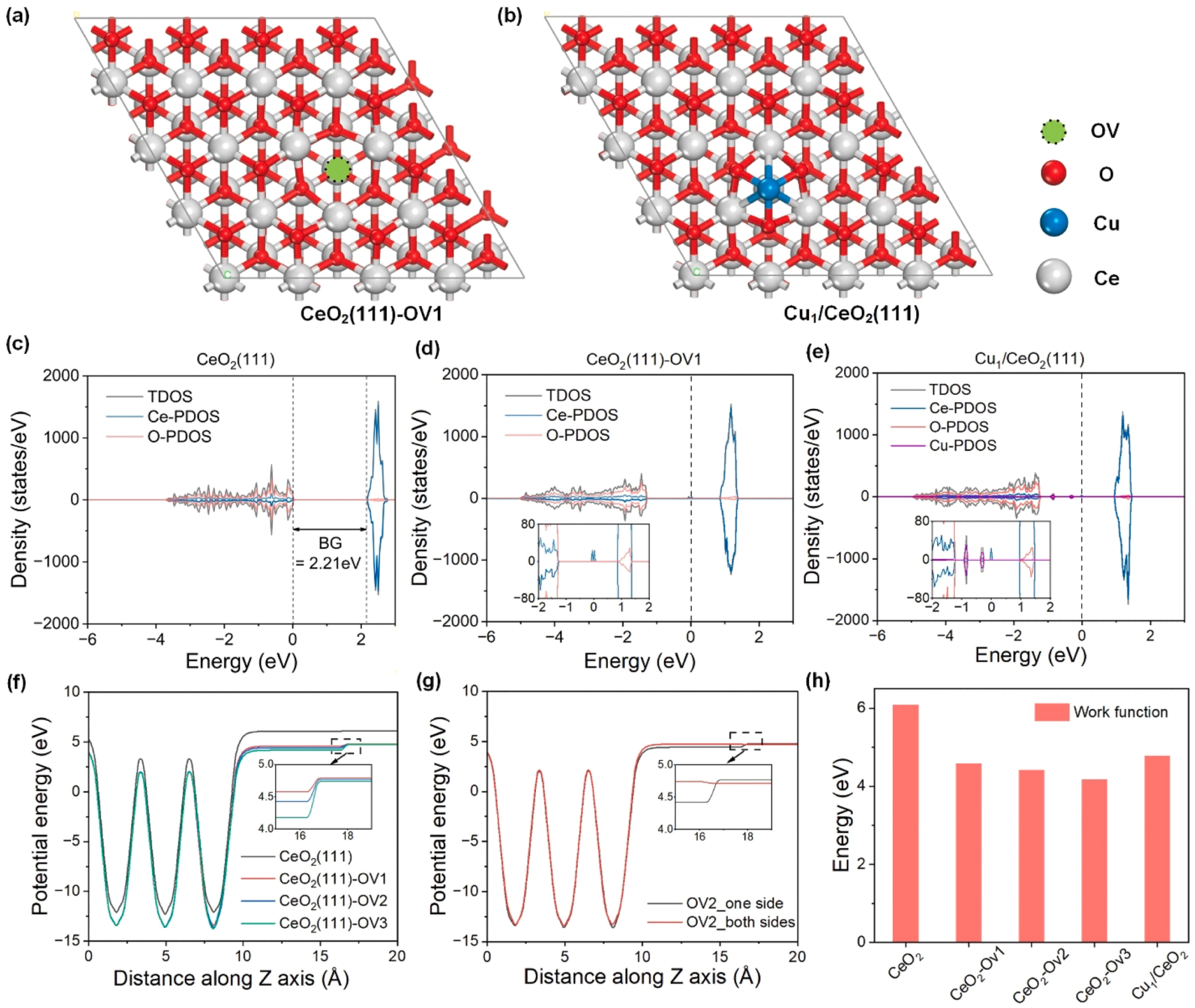

Fig. 10. (a, b) Optimized surface models of defective $CeO_2(111)$ with a surface OV ($CeO_2(111)$–OV1) and the single-atom Cu–modified surface ($Cu_1/CeO_2(111)$), respectively. Ce, O, Cu atoms and the OV are represented by gray, red, blue spheres and a green dashed circle, respectively. (c – e) Total and projected density of states (TDOS and PDOS) of pristine $CeO_2(111)$, $CeO_2(111)$–OV1, and $Cu_1/CeO_2(111)$. The Fermi level is set to 0 eV. (f, g) Planar-averaged electrostatic potential along the surface normal (z direction). The Fermi level is set to 0 eV. (f) for different OV concentrations (OV1 – OV3) on $CeO_2(111)$, and (g) for $CeO_2(111)$ with two OVs located on one side or on both sides of the slab. The insets in (f, g) highlight the vacuum-level region to illustrate variations in the surface dipole and WF-related potential shifts. (h) Comparison of the WF for increased OV concentration (OV1–OV3) and Cu introduction.

this reasoning: despite the further drop in BET surface area (from 26 m^2/g for 3 wt% to 19 m^2/g for 6 wt%), the CO_2 conversion was not significantly altered (18.6 ± 0.3% for 3 wt% and 19.3 ± 0.5% for 6 wt %). This trend confirms that the specific surface area is not the dominant factor determining the CO_2 conversion in this system.

Overall, this work shows that for plasma-catalytic hydrogenation in a packed bed DBD reactor, the modification of the discharge behavior upon packing the reactor remains the dominant influence. This impacts the gas phase chemistry, while the contribution of surface reactions remains minimal. These findings align with existing literature and likely stem from the short lifetimes of plasma-activated species, their inability to penetrate catalyst pores [55], and the relatively large inter-pellet gaps characteristic for conventional packed bed DBD designs [1]. To achieve true plasma-catalytic synergy, research should focus on enhancing the transport of short-lived plasma-activated species to the catalytic surface by minimizing the gas phase volumes.

The limited contribution of surface reactions may also be attributed to the relatively low operating temperature of our system compared to thermal catalysis. Our TPR results show that temperatures above 350 °C are required for OV formation on CeO_2, while Cu/CeO_2 requires temperatures above 100 °C on Cu/CeO_2. Due to the high spatial and temporal dynamicity of DBD plasmas, accurately determining whether the catalyst reaches such temperatures to replenish surface OVs remains a challenge. [1]. However, XPS of the spent samples (Figure S14-S18) reveals a measurable increase in OV concentration after reaction, possibly due to local hotspots or H_2 dissociation within the plasma. Consequently, it appears that the formation of OVs is likely not the main bottleneck for surface reactions in this system.

4. Conclusion

We studied the influence of the surface OV concentration in various CeO_2 samples on their plasma-catalytic activity for CO_2 hydrogenation. Contrary to the common expectation that a reverse MvK mechanism and radical O scavenging by OV enhance CO_2 conversion, our findings show the opposite trend: samples with a higher surface OV concentration exhibit lower CO_2 conversion. A detailed analysis of the discharge characteristics shows that the microdischarge quantity, which is a quantification of both the intensity and number of microdischarges, decreases with increasing OV concentration. DFT calculations indicate that OVs on CeO_2 lower the WF, modifying the fundamental discharge processes. The lower microdischarge quantity correlates with the observed decline in CO_2 conversion. Loading CeO_2 with Cu nanoparticles leads to an additional decline in CO_2 conversion, consistent with the further decrease in microdischarge quantity. The DFT results attribute this to the further decrease of the WF due to Cu introduction. Our findings highlight that discharge characteristics depend sensitively on the catalyst material and its oxidation state and therefore must be considered explicitly in plasma catalysis studies. Surface chemistry effects cannot be interpreted independently of their concomitant effect on the plasma. Moreover, in conventional packed bed DBD reactors, product formation is dominated by non-selective gas-phase chemistry.

CRediT authorship contribution statement

Joran Van Turnhout: Writing – original draft, Visualization, Methodology, Investigation, Formal analysis, Data curation, Conceptualization. **Wouter Van Hoey:** Writing – original draft, Visualization, Methodology, Investigation, Formal analysis, Data curation, Conceptualization. **Shangkun Li:** Writing – original draft, Visualization, Methodology, Investigation, Formal analysis, Data curation, Conceptualization. **Robin De Meyer:** Writing – review & editing, Visualization, Methodology, Investigation, Formal analysis, Data curation. **Morgane Van Hove:** Writing – review & editing, Visualization, Investigation, Formal analysis, Data curation. **Thomas Salens:** Writing – review & editing, Investigation, Formal analysis, Data curation. **Johan Verbeeck:** Writing – review & editing, Supervision, Funding acquisition. **Sara Bals:** Writing – review & editing, Supervision, Funding acquisition. **Bart Partoens:** Writing – review & editing, Supervision, Funding acquisition. **Emiel JM Hensen:** Writing – review & editing, Supervision, Funding acquisition. **Pegie Cool:** Writing – review & editing, Supervision, Funding acquisition, Conceptualization. **Annemie Bogaerts:** Writing – review & editing, Supervision, Funding acquisition, Conceptualization.

Declaration of Competing Interest

The authors declare the following financial interests/personal relationships which may be considered as potential competing interests: Joran Van Turnhout reports financial support was provided by European Research Council. Shangkun Li reports equipment, drugs, or supplies was provided by Flemish Supercomputer Center. If there are other authors, they declare that they have no known competing financial interests or personal relationships that could have appeared to influence the work reported in this paper

Acknowledgments

This research was supported by the European Research Council (ERC) under the European Union's Horizon 2020 research and innovation programme (grant agreement No 810182 – SCOPE ERC Synergy project), the UAntwerp BOF GOA (project ID 36083) and the long-term structural funding of the Centers of Excellence PLASMA and NanoLight at UAntwerp (Methusalem FFB15001A, FFB15001B and FFB15001C). The research was partially carried out with the X-ray diffraction equipment funded by the UA BOF research infrastructure (project ID 41358). The computational resources and services used in this work were provided by the HPC core facility CalcUA of the Universiteit Antwerpen, and VSC (Flemish Supercomputer Center). Finally, we also gratefully acknowledge Doran Platteau for the execution of some of the experiments.

Appendix A. Supporting information

Supplementary data associated with this article can be found in the online version at doi:10.1016/j.jcou.2026.103393.

Data availability

Data will be made available on request.

References

[1] J. Van Turnhout, K. Rouwenhorst, L. Lefferts, A. Bogaerts, Plasma catalysis: what is needed to create synergy? EES Catal. 3 (4) (2025) 669–693, https://doi.org/10.1039/d5ey00027k.

[2] E.C. Neyts, K.K. Ostrikov, M.K. Sunkara, A. Bogaerts, Plasma catalysis: synergistic effects at the nanoscale, Chem. Rev. 115 (24) (2015) 13408–13446, https://doi.org/10.1021/acs.chemrev.5b00362.

[3] X. Tu, J.C. Whitehead, Plasma-catalytic dry reforming of methane in an atmospheric dielectric barrier discharge: understanding the synergistic effect at low temperature, Appl. Catal. B Environ. 125 (2012) 439–448, https://doi.org/10.1016/j.apcatb.2012.06.006.

[4] A. Parastaev, V. Muravev, E.H. Osta, A.J.F. van Hoof, T.F. Kimpel, N. Kosinov, E.J. M. Hensen, Boosting CO_2 hydrogenation via size-dependent metal–support interactions in cobalt/ceria-based catalysts, Nat. Catal. 3 (6) (2020) 526–533, https://doi.org/10.1038/s41929-020-0459-4.

[5] R. Kopelent, J.A. van Bokhoven, J. Szlachetko, J. Edebeli, C. Paun, M. Nachtegaal, O.V. Safonova, Catalytically active and spectator $Ce^{(3+)}$ in Ceria-supported metal catalysts, Angew. Chem. Int. Ed. Engl. 54 (30) (2015) 8728–8731, https://doi.org/10.1002/anie.201503022.

[6] B. Loenders, R. Michiels, A. Bogaerts, Is a catalyst always beneficial in plasma catalysis? Insights from the many physical and chemical interactions, J. Energy Chem. 85 (2023) 501–533, https://doi.org/10.1016/j.jechem.2023.06.016.

[7] R. De Meyer, Y. Gorbanev, R.-G. Ciocarlan, P. Cool, S. Bals, A. Bogaerts, Importance of plasma discharge characteristics in plasma catalysis: dry reforming of methane vs. ammonia synthesis, Chem. Eng. J. 488 (2024), https://doi.org/10.1016/j.cej.2024.150838.

[8] C. Ndayirinde, Y. Gorbanev, R.-G. Ciocarlan, R. De Meyer, A. Smets, E. Vlasov, S. Bals, P. Cool, A. Bogaerts, Plasma-catalytic ammonia synthesis: Packed catalysts act as plasma modifiers, Catal. Today 419 (2023), https://doi.org/10.1016/j.cattod.2023.114156.

[9] P. Mars, D.W. van Krevelen, Oxidations carried out by means of vanadium oxide catalysts, Chem. Eng. Sci. 3 (1954) 41–59, https://doi.org/10.1016/s0009-2509(54)80005-4.

[10] C. Yang, Y. Lu, L. Zhang, Z. Kong, T. Yang, L. Tao, Y. Zou, S. Wang, Defect engineering on CeO_2-based catalysts for heterogeneous catalytic applications, Small Struct. 2 (12) (2021), https://doi.org/10.1002/sstr.202100058.

[11] T. Montini, M. Melchionna, M. Monai, P. Fornasiero, Fundamentals and catalytic applications of CeO_2-based materials, Chem. Rev. 116 (10) (2016) 5987–6041, https://doi.org/10.1021/acs.chemrev.5b00603.

[12] A. Parastaev, N. Kosinov, E.J.M. Hensen, Mechanistic study of catalytic CO_2 hydrogenation in a plasma by operando DRIFT spectroscopy, J. Phys. D Appl. Phys. 54 (26) (2021), https://doi.org/10.1088/1361-6463/abeb96.

[13] Z. Ning, L. Wen, R. Li, K. Xin, P. Liu, L. Liu, Y. Sun, Y. Zhu, P. Ning, Oxygen vacancy-enriched Cu/CeO_2–ZrO_2 catalyst with highly dispersed Cu^0 towards plasma catalytic advanced CO_2 utilization, J. Clean. Prod. 442 (2024), https://doi.org/10.1016/j.jclepro.2024.141010.

[14] O.V. Golubev, P.S. Il'chuk, A.A. Sadovnikov, A.L. Maximov, Carbon dioxide utilization using plasma reactor packed with magnesia-ceria catalysts with various morphology, Pet. Chem. 63 (9) (2023) 1097–1109, https://doi.org/10.1134/s0965544123080066.

[15] B. Ashford, Y. Wang, C.-K. Poh, L. Chen, X. Tu, Plasma-catalytic conversion of CO_2 to CO over binary metal oxide catalysts at low temperatures, Appl. Catal. B Environ. 276 (2020), https://doi.org/10.1016/j.apcatb.2020.119110.

[16] C. Cheng, Y. Wang, J. Wang, H. Xu, W. Huang, Z. Liu, W. Li, Y. Li, Z. Qu, X. Tu, N. Yan, Oxygen-vacancy-engineered Pd-WO_3–x for enhanced plasma-catalyzed CO_2 hydrogenation to CO, ACS Catal. (2026), https://doi.org/10.1021/acscatal.5c07524.

[17] N. Merino, M. Mikhail, X. Duten, M. Tatoulian, S. Ognier, Reliable quantification of liquid oxygenated products in CO_2/CH_4 plasma-catalytic conversion, Energy Convers. Manag 352 (2026), https://doi.org/10.1016/j.enconman.2026.121115.

[18] W. Van Hoey, A. Rokicińska, M. Dębosz, I. Majewska, P. Kuśtrowski, P. Cool, Preparation of noble metal-free porous CuO–ceria and zirconia mixed oxide catalysts using the ammonia driven deposition precipitation method for toluene combustion, Mater. Adv. 5 (17) (2024) 6983–6995, https://doi.org/10.1039/d4ma00324a.

[19] X. Guo, A. Yin, W.-L. Dai, K. Fan, One pot synthesis of ultra-high copper contented Cu/SBA-15 material as excellent catalyst in the hydrogenation of dimethyl oxalate to ethylene glycol, Catal. Lett. 132 (1-2) (2009) 22–27, https://doi.org/10.1007/s10562-009-0043-7.

[20] Q. Xin, A. Papavasiliou, N. Boukos, A. Glisenti, J.P.H. Li, Y. Yang, C. P. Philippopoulos, E. Pulakis, F.K. Katsaros, V. Meynen, P. Cool, Preparation of CuO/SBA-15 catalyst by the modified ammonia driven deposition precipitation method with a high thermal stability and an efficient automotive CO and hydrocarbons conversion, Appl. Catal. B Environ. 223 (2018) 103–115, https://doi.org/10.1016/j.apcatb.2017.03.071.

[21] H. Idriss, On the wrong assignment of the XPS O1s signal at 531–532 eV attributed to oxygen vacancies in photo- and electro-catalysts for water splitting and other materials applications, Surf. Sci. 712 (2021), https://doi.org/10.1016/j.susc.2021.121894.

[22] T. Skála, F. Šutara, K.C. Prince, V. Matolín, Cerium oxide stoichiometry alteration via Sn deposition: influence of temperature, J. Electron Spectrosc. Relat. Phenom. 169 (1) (2009) 20–25, https://doi.org/10.1016/j.elspec.2008.10.003.

[23] S. Kato, M. Ammann, T. Huthewelker, C. Paun, M. Lampimäki, M.-T. Lee, M. Rothensteiner, J.A. van Bokhoven, Quantitative depth profiling of Ce$^{(3+)}$ in Pt/CeO$_2$ by in situ high-energy XPS in a hydrogen atmosphere, Phys. Chem. Chem. Phys. 17 (7) (2015) 5078–5083, https://doi.org/10.1039/c4cp05643d.

[24] B. Wanten, R. Vertongen, R. De Meyer, A. Bogaerts, Plasma-based CO$_2$ conversion: How to correctly analyze the performance? J. Energy Chem. 86 (2023) 180–196, https://doi.org/10.1016/j.jechem.2023.07.005.

[25] F.J.J. Peeters, M.C.M. van de Sanden, The influence of partial surface discharging on the electrical characterization of DBDs, Plasma Sources Sci. Technol. 24 (1) (2014), https://doi.org/10.1088/0963-0252/24/1/015016.

[26] G. Kresse, J. Furthmüller, Efficiency of ab-initio total energy calculations for metals and semiconductors using a plane-wave basis set, Comput. Mater. Sci. 6 (1) (1996) 15–50, https://doi.org/10.1016/0927-0256(96)00008-0.

[27] G. Kresse, J. Furthmuller, Efficient iterative schemes for ab initio total-energy calculations using a plane-wave basis set, Phys. Rev. B Condens. Matter 54 (16) (1996) 11169–11186, https://doi.org/10.1103/physrevb.54.11169.

[28] G. Kresse, J. Hafner, Ab initio molecular dynamics for liquid metals, Phys. Rev. B Condens. Matter 47 (1) (1993) 558–561, https://doi.org/10.1103/physrevb.47.558.

[29] J.P. Perdew, K. Burke, M. Ernzerhof, Generalized gradient approximation made simple, Phys. Rev. Lett. 77 (18) (1996) 3865–3868, https://doi.org/10.1103/PhysRevLett.77.3865.

[30] P.E. Blochl, Projector augmented-wave method, Phys. Rev. B Condens. Matter 50 (24) (1994) 17953–17979, https://doi.org/10.1103/physrevb.50.17953.

[31] G. Kresse, D. Joubert, From ultrasoft pseudopotentials to the projector augmented-wave method, Phys. Rev. B 59 (3) (1999) 1758–1775, https://doi.org/10.1103/PhysRevB.59.1758.

[32] S.L. Dudarev, G.A. Botton, S.Y. Savrasov, C.J. Humphreys, A.P. Sutton, Electron-energy-loss spectra and the structural stability of nickel oxide:an LSDA+U study, Phys. Rev. B 57 (3) (1998) 1505–1509, https://doi.org/10.1103/PhysRevB.57.1505.

[33] L. Chen, I.A.W. Filot, E.J.M. Hensen, Computational study of CO2 methanation on Ru/CeO$_2$ model surfaces: on the impact of Ru doping in CeO2, ACS Catal. 13 (23) (2023) 15230–15247, https://doi.org/10.1021/acscatal.3c03742.

[34] Z.-Q. Huang, L.-P. Liu, S. Qi, S. Zhang, Y. Qu, C.-R. Chang, Understanding all-solid frustrated-lewis-pair sites on CeO2 from theoretical perspectives, ACS Catal. 8 (1) (2017) 546–554, https://doi.org/10.1021/acscatal.7b02732.

[35] Z.-Q. Huang, T. Zhang, C.-R. Chang, J. Li, Dynamic frustrated lewis pairs on ceria for direct nonoxidative coupling of methane, ACS Catal. 9 (6) (2019) 5523–5536, https://doi.org/10.1021/acscatal.9b00838.

[36] S. Grimme, J. Antony, S. Ehrlich, H. Krieg, A consistent and accurate ab initio parametrization of density functional dispersion correction (DFT-D) for the 94 elements H-Pu, J. Chem. Phys. 132 (15) (2010) 154104, https://doi.org/10.1063/1.3382344.

[37] L. Gerward, J.Staun Olsen, Powder diffraction analysis of cerium dioxide at high pressure, Powder Diffr. 8 (2) (1993).

[38] J.F. Xu, W. Ji, Z.X. Shen, W.S. Li, S.H. Tang, X.R. Ye, D.Z. Jia, X.Q. Xin, Raman spectra of CuO nanocrystals,, J. Raman Spectrosc. 30 (5) (1999) 413–415, https://doi.org/10.1002/(sici)1097-4555(199905)30:5<413::Aid-jrs387>3.0.Co;2-n.

[39] C. Ren, R. Yang, Y. Li, H. Wang, Modulating of facets-dependent oxygen vacancies on ceria and its catalytic oxidation performance, Res. Chem. Inter. 45 (5) (2019) 3019–3032, https://doi.org/10.1007/s11164-019-03776-6.

[40] J. Zhu, Y. Su, J. Chai, V. Muravev, N. Kosinov, E.J.M. Hensen, Mechanism and nature of active sites for methanol synthesis from CO/CO$_2$ on Cu/CeO$_2$, ACS Catal. 10 (19) (2020) 11532–11544, https://doi.org/10.1021/acscatal.0c02909.

[41] D. Cai, B. Chen, Z. Huang, X. Zeng, J. Xiao, S.-F. Zhou, G. Zhan, Metal oxide/CeO$_2$ nanocomposites derived from Ce-benzene tricarboxylate (Ce-BTC) adsorbing with metal acetylacetonate complexes for catalytic oxidation of carbon monoxide, RSC Adv. 11 (34) (2021) 21057–21065, https://doi.org/10.1039/d1ra03319k.

[42] L. Lefferts, Leveraging expertise in thermal catalysis to understand plasma catalysis, Angew. Chem. 136 (10) (2024), https://doi.org/10.1002/ange.202305322.

[43] T. Thajudheen, A.G. Dixon, S. Gardonio, I. Arcon, M. Valant, Oxygen vacancy-related cathodoluminescence quenching and polarons in CeO$_2$, J. Phys. Chem. C. 124 (37) (2020) 19929–19936, https://doi.org/10.1021/acs.jpcc.0c04631.

[44] L. Chen, I.A.W. Filot, E.J.M. Hensen, Elucidation of the reverse water–gas shift reaction mechanism over an isolated Ru atom on CeO2(111), J. Phys. Chem. C. 127 (41) (2023) 20314–20324, https://doi.org/10.1021/acs.jpcc.3c03983.

[45] W. Ji, N. Wang, X. Chen, Q. Li, K. Lin, J. Deng, J. Chen, X. Xing, Effects of subsurface oxide on Cu$_1$/CeO$_2$ single-atom catalysts for CO oxidation: a theoretical investigation, Inorg. Chem. 61 (26) (2022) 10006–10014, https://doi.org/10.1021/acs.inorgchem.2c00879.

[46] B. Choudhury, A. Choudhury, Ce^{3+} and oxygen vacancy mediated tuning of structural and optical properties of CeO$_2$ nanoparticles, Mater. Chem. Phys. 131 (3) (2012) 666–671, https://doi.org/10.1016/j.matchemphys.2011.10.032.

[47] Y. Huang, C.-F. Yan, C.-Q. Guo, Y. Shi, Experimental and first-principles DFT study on oxygen vacancies on cerium dioxide and its effect on enhanced photocatalytic hydrogen production, Int. J. Hydrog. Energy 41 (19) (2016) 7919–7926, https://doi.org/10.1016/j.ijhydene.2015.10.151.

[48] H.-H. Kim, Y. Teramoto, A. Ogata, Time-resolved imaging of positive pulsed corona-induced surface streamers on TiO$_2$ and γ-Al$_2$O$_3$-supported Ag catalysts, J. Phys. D Appl. Phys. 49 (41) (2016), https://doi.org/10.1088/0022-3727/49/41/415204.

[49] M.A. Cazalilla, N. Lorente, R.D. Muiño, J.P. Gauyacq, D. Teillet-Billy, P. M. Echenique, Theory of Auger neutralization and deexcitation of slow ions at metal surfaces, Phys. Rev. B 58 (20) (1998) 13991–14006, https://doi.org/10.1103/PhysRevB.58.13991.

[50] F. Massines, N. Gherardi, N. Naudé, P. Ségur, Recent advances in the understanding of homogeneous dielectric barrier discharges, Eur. Phys. J. AP 47 (2) (2009), https://doi.org/10.1051/epjap/2009064.

[51] M.A. More, D.S. Joag, R.G. Forbes, Field Electron Emission from Nanomaterials, in: B. Bhushan (Ed.), Encyclopedia of Nanotechnology, Springer, Dordrecht, 2015, pp. 1–23, ch. Chapter 35-2.

[52] J. Kruszelnicki, K.W. Engeling, J.E. Foster, Z. Xiong, M.J. Kushner, Propagation of negative electrical discharges through 2-dimensional packed bed reactors, J. Phys. D Appl. Phys. 50 (2) (2017), https://doi.org/10.1088/1361-6463/50/2/025203.

[53] W. Wang, H.-H. Kim, K. Van Laer, A. Bogaerts, Streamer propagation in a packed bed plasma reactor for plasma catalysis applications, Chem. Eng. J. 334 (2018) 2467–2479, https://doi.org/10.1016/j.cej.2017.11.139.

[54] R. Snoeckx, R. Aerts, X. Tu, A. Bogaerts, Plasma-based dry reforming: a computational study ranging from the nanoseconds to seconds time scale, J. Phys. Chem. C. 117 (10) (2013) 4957–4970, https://doi.org/10.1021/jp311912b.

[55] Q.-Z. Zhang, A. Bogaerts, Propagation of a plasma streamer in catalyst pores, Plasma Sources Sci. Technol. 27 (3) (2018), https://doi.org/10.1088/1361-6595/aab47a.